# Numerical Study of Two-Phase Granular Flow for Process Equipment

**R. Djebbar**
e-mail: reda.djebbar@nrc.ca

**S. B. Beale**
Mem. ASME
e-mail: steven.beale@nrc.ca

**M. Sayed**
e-mail: mohamed.sayed@nrc.ca

National Research Council,
Montreal Road,
Ottawa, Ontario K1A 0R6, Canada

*This paper reports on a research program of modeling multi-phase granular flow. Both single-phase granular flow and two-phase liquid/granular flow in a pressure vessel were considered. For the latter case, detailed results based on a viscous/Mohr-Coulomb closure were compared to existing formulations. Idealized test cases indicated that the numerical procedure is sound. Subsequent simulations of two-phase flow using realistic geometries and boundary conditions showed that the pressure distribution in the solid phase is fundamentally different for the Mohr-Coulomb system than for the conventional system. The effect of the angle of internal friction, geometry, and other parameters is discussed.* [S0094-9930(00)01204-X]

## Introduction

Flow of granular materials within a viscous fluid is a subject with many important applications in various industries. Figure 1 illustrates an experimental reactor-vessel used to process wood chips into pulp. Solid chips and liquid material are introduced at the top, and removed at the bottom of the pressure vessel. There are four main regions: An impregnation zone, followed by (from top-to-bottom) heating, cooking, and washing zones. The unconsolidated porous matrix of solid particles is saturated with free liquid in the upper impregnation zone. The chips are then brought to the required cooking temperature in the heating zone. Chemical delignification of the wood fibers occurs in the cooking stage, while the chips are cooled and washed in the lower zone. Additional liquid, necessary for cooking, is introduced at three locations in the apparatus; spent fluid being extracted at two sets of screens in the outer wall. Smooth flow of the granular material within the vessel, under the action of gravity and fluid drag, is critical to the successful operation of the apparatus, especially in the washing zone, where a counterflow regime exists. Hanging of the chip column, or plugging of the extraction screens could lead to time-consuming and expensive downtime.

In view of the elevated pressures and temperatures, caustic environment, and complex nature of the flow, performing even the simplest experiments is difficult or impossible. Under these circumstances, computational fluid dynamics (CFD) can convey important information to the manufacturer and operator of the equipment. Chemical kinetics, heat, and mass transfer are considered beyond the scope of this paper, which is concerned only with the mechanics of the solid and liquid phases, knowledge of which is of paramount importance to the operator.

Härkönen [1,2] was among the first to attempt numerical modeling of such a system. He considered two-dimensional (2-D) steady-state flow within the axisymmetric reactor illustrated in Fig. 1. Fluid flow within the isotropic porous media was described by the Ergun-modified form of Darcy's law Scheidegger [3]. Terms due to confining and pore pressure, as well as Darcy friction and gravity, were constructed in a force balance. Härkönen's scheme involved the solution for a harmonic potential satisfying continuity, followed by the iterative solution for the solid bed (intergranular) pressure, volume fraction, phase velocities, and Darcian interphase slip coefficient. Härkönen's method was based on the notion that a solid pressure, $P$, distinct from the fluid pressure, $p$, was present; no shear forces were permitted, however, within the granular material, other than at the wall, i.e., the bulk material was treated as an inviscid fluid. The scheme has formed the basis for subsequent calculations, e.g., Michelsen and Foss [4], who considered transient one-dimensional (1-D) two-phase flow in an industrial digester, and treated and solid material as a Newtonian fluid with a kinematic viscosity of $10^{-3}$ ($m^2/s$). Chip and liquid heights were allowed to vary; however, radial momentum was presumed insignificant in comparison to axial momentum. Saltin [5] also considered a 1-D flow model. The Härkönen scheme suffers from a number of restrictions: (*i*) The method is based on a static balance, i.e., creeping flow and inertial terms are excluded. (*ii*) Because a scalar potential is employed, boundary

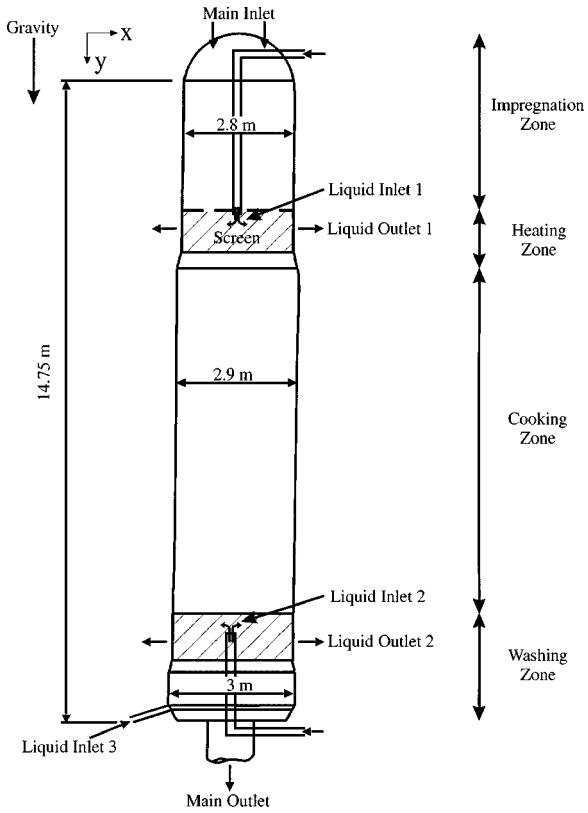


**Fig. 1 Schematic of the reactor vessel used in the study**

Contributed by the Pressure Vessels and Piping Division and presented at the Pressure Vessels and Piping Conference, Boston, Massachusetts, August 1–5, 1999, of THE AMERICAN SOCIETY OF MECHANICAL ENGINEERS. Manuscript received by the PVP Division, October 1999; revised manuscript received February 2000. Technical Editor: S. Y. Zamrik.

layer effects [3] cannot be accounted for. (*iii*) The rheology of the chip column is idealized. (*iv*) The algorithm employed is highly specialized.

The goals of this study are to: (*a*) develop a model of 2-D single and two-phase granular flow with standard CFD methods and codes; (*b*) validate the method against previous numerical work; (*c*) introduce a more realistic rheology, which includes the frictional behavior of the solid phase; (*d*) conduct parametric studies to ascertain the effects of the frictional properties of the solid phase on the flow.

**Rheology of the Solid Phase.** Flowing granular materials are known to behave differently from viscous fluids. The significant feature is that the shear stresses are proportional to the normal stresses. Such frictional properties give rise to one of the well-known observations concerning pressure distribution in bins. Brown and Richards [6] considered the equilibrium of vertical forces on a section of the granular material to show that the pressure on the walls of a bin increase linearly with depth, only near the top (Janssen's equation). The resulting vertical distribution of the pressure follows an exponential profile, tending to a constant maximum value that does not increase with further increase of depth. Granular materials are commonly described by a Mohr-Coulomb criterion as follows:

$$\tau = c + \sigma \sin \phi \tag{1}$$

where $\tau$ and $\sigma$ are the shear and normal stress on the failure plane, $c$ is the cohesion term, and $\phi$ is the angle of internal friction. The angle, $\phi$, is approximately equal to the angle of repose of the granular material. For 2-D Cartesian coordinates, the stress relations are

$$\sigma_{11} = -P(1 + \sin \phi \cos 2\psi) \tag{2}$$

$$\sigma_{22} = -P(1 - \sin \phi \cos 2\psi) \tag{3}$$

$$\tau_{12} = -P \sin \phi \sin 2\psi \tag{4}$$

where $\sigma_{11}, \sigma_{22}, \tau_{12}$ are the normal and shear stresses, $\psi$ is the angle between the major principal stress $\sigma_1$ and the $x_1$-axis, and the solid pressure, $P$, is,

$$P = -\left(\frac{\sigma_{\mathrm{I}} + \sigma_{\mathrm{II}}}{2}\right) \tag{5}$$

At low rates of deformation, it is usually assumed that granular material can be modeled as a plastic continuum, and the Mohr-Coulomb criterion is used to represent the frictional behavior; Drucker and Prager [7]. There have since been a large amount of related investigations. Most of the relevant results may be found in soil mechanics textbooks, e.g., Scott [8]. At high rates of deformation, flowing granular materials exhibit a behavior that is somewhat different. Particle-particle collisions give rise to stresses that depend on the magnitude of the rate of deformation; i.e., of a turbulent nature. Savage [9] gives a review of that behavior. There is no indication that the present problem requires the latter; consequently, we incorporate the frictional behavior of the solid phase by employing a plasticity approach representing the slow deformation regime. The impact on performance of using models for the high rate regime is left for future investigations. Such work may also consider the theory of Savage [10], which incorporates particle fluctuations in a plasticity framework.

## Governing Equations

Two distinct classes of problem are considered in the present work. (*i*) The motion of incompressible bulk granular material. Interstitial fluid effects are assumed negligible. The objective is to verify that the present numerical scheme can deal with plastic rheology. (*ii*) The simultaneous motion of both granular and interstitial viscous fluid phases, and the coupling between them. This case is considered in order to examine flow conditions in the industrial pressure vessel.

**Incompressible Single-Phase Granular Flow.** The continuity and momentum equations of the bulk granular material may be written as follows:

$$\nabla \cdot (\rho \mathbf{u}) = 0 \tag{6}$$

$$\nabla \cdot (\rho \mathbf{u}; \mathbf{u}) = \rho g + \nabla \cdot \bar{\bar{\sigma}} \tag{7}$$

where $\mathbf{u}$ is the velocity, $\rho$ is an effective density, $\mathbf{g}$ is the acceleration due to gravity, and $\bar{\bar{\sigma}}$ is the stress tensor. Tensile normal stresses are considered positive in Eqs. (6) and (7). The relationship between the stress and the rate of deformation may be expressed as[1]

$$\sigma_{ij} = -P\delta_{ij} + 2\eta d_{ij} \tag{8}$$

where $d_{ij} = 1/2(u_{i'j} + u_{j'i})$ are the components of the rate of deformation, $P$ is the pressure, see Eq. (5), and $\eta$ is a solid phase shear viscosity. Bulk viscosity is considered negligible in Eq. (8). The Mohr-Coulomb criterion and associated flow rule are introduced into the flow algorithm by giving the shear viscosity, $\eta$, the following value:

$$\eta = \frac{P \sin \phi}{\Delta} \tag{9}$$

The rate of deformation, $\Delta$, is given by

$$\Delta = \max(|d_{\mathrm{I}} - d_{\mathrm{II}}|, d_0) \tag{10}$$

where $d_{\mathrm{I}}$ and $d_{\mathrm{II}}$ are principle values of the deformation gradient tensor, and $d_0$ is a threshold rate of deformation. For large rates of deformation, $\Delta > d_0$, the rheology is plastic, with stresses independent of the magnitude of the rate of deformation components. For $\Delta \leqslant d_0$, the shear viscosity is constant, and the deformation is viscous. Thus, the present model employs a viscous-plastic formulation to approximate rigid-plastic conditions. The threshold rate of deformation, $d_0$, is assigned a very small value in order to maintain a predominantly plastic deformation. Equations (6) to (10), together with the appropriate boundary conditions, are sufficient to determine the velocities and components of the stress tensor.

**Compressible Two-Phase Fluid/Granular Flow.** For this type of analysis, we add the equations of motion of the fluid phase, terms describing the coupling between solid and fluid phases, and an equation-of-state for the solid phase (needed to model the bulk compressibility of the granular material). The continuity and momentum equations for the fluid phase are

$$\nabla \cdot (r_f \rho_f \mathbf{u}_f) = 0 \tag{11}$$

$$\nabla \cdot (r_f \rho_f \mathbf{u}_f; \mathbf{u}_f) = r_f \rho_f \mathbf{g} - r_f \nabla p + \nabla \cdot (\nabla r_f \mu \mathbf{u}_f) + k'(\mathbf{u}_f - \mathbf{u}_s) \tag{12}$$

where $r_f$ is the fluid volume fraction, $0 \leqslant r_f \leqslant 1$, $\rho_f$ and $\mathbf{u}_f$ are liquid velocity and density, respectively, $\mu$ is the fluid viscosity, and $p$ is a fluid or pore pressure. The interphase slip coefficient, $k'$, is given by

$$k' = r_f \frac{\mu}{k} + \rho_f r_f^2 b |\mathbf{u}_f - \mathbf{u}_s| \tag{13}$$

where $k$ is permeability, and $b$ is Forchheimer's constant [3]. For the solid phase, i.e., the bulk granular material

$$\nabla \cdot (r_s \rho_s \mathbf{u}_s) = 0 \tag{14}$$

$$\nabla \cdot (r_s \rho_s \mathbf{u}_s; \mathbf{u}_s) = r_s \rho_s \mathbf{g} - r_s \nabla p + \nabla \cdot (r_s \bar{\bar{\sigma}}) + k'(\mathbf{u}_s - \mathbf{u}_f) \tag{15}$$

where $r_s = 1 - r_f$ is the solid volume fraction and $\rho_s$ and $\mathbf{u}_s$ refer to the solid phase. The components of the solid phase stress tensor

[1]Cartesian tensor notation is adopted for reasons of brevity. The vector forms in Cartesian and polar coordinates may easily be derived.

$\bar{\bar{\sigma}}$ are given in Eq. (8). For compressible flow, the solid (granular) pressure, $P$, is related to the volume fraction according to an equation-of-state, or compressibility equation

$$r_s = A + BP^m \tag{16}$$

for $P \geq 0$. The fluid pressure, $p$, is solved for, but the solid pressure, $P$, is obtained algebraically, by inversion of Eq. (16) as

$$P = \frac{10^4}{0.831 - 0.139 \ln \kappa} (r_s - 0.356)^{1.695} \tag{17}$$

from Härkönen [2], with a constant value of $\kappa = 195$, Michelsen and Foss [4], and $r_s > 0.356$. The reader will note that while the fluid pressure, $p$, acts on both fluid and solid, the solid pressure, $P$, has no effect upon the fluid. Thus, $p$ is sometimes referred to as a ''shared'' pressure.

Both incompressible single-phase granular flow, and compressible two-phase fluid/granular flow were considered in this study. For the former case a finite-volume method based on the SIMPLE (semi-implicit method for pressure linked equations) algorithm, Patankar [11], may be employed. For the latter case, an IPSA (interphase slip algorithm), Spalding [12], was used. The research-oriented CFD code PHOENICS, was modified to compute (*a*) $\eta$ according to Eq. (9) (all cases), (*b*) $k'$ according to Eq. (13) (two-phase cases) and $P$ according to Eq. (17) (compressible cases), at the end of each ''sweep'' or iterative cycle, and (*c*) boundary conditions, as described in the forthcoming paragraph.

**Boundary and Initial Conditions.** Treatment of a granular flow at a wall is as follows. The shear stress on the wall is assumed to be

$$\tau_w = \frac{P \sin \phi_w}{\Delta} \frac{\partial u}{\partial n} \tag{18}$$

where $\partial u / \partial n$ is the velocity gradient, $\phi_w$ is the angle of friction between material and wall, $0 \leq \phi_w \leq \phi$, and $\Delta$ is computed with Eq. (10). By changing $\phi_w$, the wall shear stress may thus be varied from no slip to pure slip.

The liquid flow is dominated by gravity and Darcy (inter-phase) friction, in the inertial regime, so wall effects were not considered. Other boundary prescriptions are straightforward; both fixed mass and momentum sources, and fixed pressure-type boundary conditions were imposed at inlets and exits, as appropriate. For two-phase flow, solid and liquid were presumed to enter with no initial inter-phase slip.

**Test Cases.** The following three cases were examined: 1) incompressible single-phase granular flow in a vertical channel, 2) two-phase viscous/viscous liquid/solid flow, 3) two-phase viscous/Mohr-Coulomb flow. Case 1 was considered in order to demonstrate the accuracy of the model, and to help clarify the results for cases 2 and 3, which involved a problem with practical industrial applications. In case 1, both frictional and frictionless granular flow are considered and compared. The effect of the angle of internal friction, and of the channel width, $D$, on the solid flow regime is analyzed. Cases 2 and 3 are both concerned with the apparatus of Fig. 1. Boundary conditions and property values are indicated in Fig. 1 and Table 1. These correspond to values given in Härkönen [1,2]. For case 2, the intergranular friction in the solid phase is presumed to be viscous, consistent with Michelsen [4], with a shear viscosity, $\eta$, corresponding to a constant kinematic viscosity of $10^{-3}\,\mathrm{m^2/s}$. For case 3, the solid-phase rheology is extended to include friction using a Mohr-Coulomb plastic yield criterion.

## Results and Discussion

**Incompressible Single-Phase Granular Flow.** Figures 2–5 show the results for gravity-driven single-phase incompressible granular flow in a straight vertical channel, Eqs. (6)–(10). The channel is open at both top and bottom. No-slip boundary conditions are imposed. The out flow is fixed corresponding to a bulk velocity of 1 mm/s and $\rho = 1132.4\,\mathrm{kg/m^3}$, while the pressure, $P$, is set to zero, at the top of the channel.

Figure 2 shows velocity vectors in the channel. The flow is predominantly in the vertical direction. Note the formation of shear layers near the channel walls, as observed in the experimental work of Savage [9], who also noted that the pluglike velocity profile in the central region of the vertical channel. Figure 3 is a

**Table 1 Boundary conditions and properties for solid and fluid phases for the problem of Fig. 3**

| Parameter | Value |
|---|---|
| Main inlet solid volume fraction, $r_s$ | 0.42 |
| Main inlet solid pressure, $P$ | 5 000 (Pa) |
| Main inlet solid velocity, $v_s$ | $2.4 \times 10^{-3}$ (m/s) |
| Main inlet liquid velocity, $v_f$ | $2.4 \times 10^{-3}$ (m/s) |
| Main inlet area | $9.8 \times 10^{-2}$ ($m^2$) |
| Liquid inlet 1, velocity, $v_f$ | 1.27 (m/s) |
| Liquid inlet 1, area, $A$ | $2.5 \times 10^{-4}$ ($m^2$) |
| Liquid inlet 2, velocity, $v_f$ | 0.95 (m/s) |
| Liquid inlet 2, area, $A$ | $2.5 \times 10^{-4}$ ($m^2$) |
| Liquid inlet 3, velocity, $v_f$ | $4.3 \times 10^{-3}$ (m/s) |
| Liquid inlet 3, area, $A$ | $5.5 \times 10^{-2}$ ($m^2$) |
| Main outlet fluid pressure, $p$ | 0 (Pa) |
| Main outlet, area, $A$ | $1.4 \times 10^{-2}$ ($m^2$) |
| Liquid outlet 1, velocity, $v_f$ | $1.7 \times 10^{-3}$ (m/s) |
| Liquid outlet 1, area, $A$ | $1.9 \times 10^{-1}$ ($m^2$) |
| Liquid outlet 2, velocity, $v_f$ | $4.24 \times 10^{-3}$ (m/s) |
| Liquid outlet 2, area, $A$ | $1.1 \times 10^{-1}$ ($m^2$) |
| Solid density, $\rho_s$ | 1132.4 ($kg/m^3$) |
| Fluid density, $\rho_f$ | 1 000 ($kg/m^3$) |
| Fluid permeability, $k$ | $\mu r_f^2 / 4.6x10^3 r_s^2$ ($m^2$) |
| Forchheimer's constant, $b$ | $3.9x10^6 r_s / \rho_f r_f^2$ (1/m) |

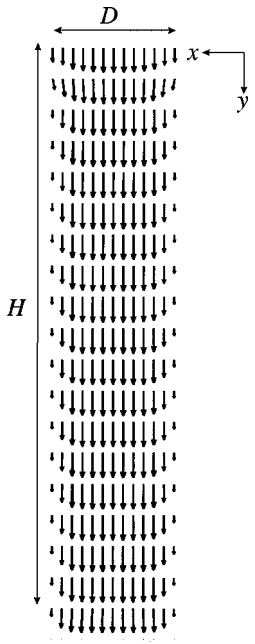


**Fig. 2 Velocity vectors for frictional granular flow, $D/H = 2{:}12$, $\phi = 20$ deg**

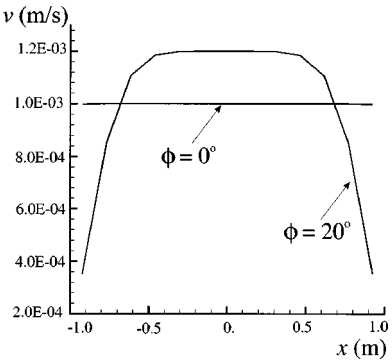


**Fig. 3 Fully developed velocity profiles for frictionless and frictional granular flow in a channel**

detail of the fully developed $v$-velocity profile. Results for both frictional, $\phi = 20$ deg, and frictionless $\phi = 0$ deg, granular material are shown. For the frictionless case, a flat profile is observed across the entire cross section of the channel, corresponding to a slip boundary condition velocity at the wall: Since $\eta_w = \eta = 0$ in Eqs. (9) and (18), there is no shear force between the particles and the wall (or each other), and therefore no mechanism for the production of friction/shear.

Figures 4 and 5 show profiles of pressure, Eq. (5), versus channel depth at the centerline. In Fig. 4, the aspect ratio $D/H$ is varied, with $H = 12$ m, and $\phi = 30$ deg. It can be seen that the pressure, $P$, increases with depth, $y$, near the top of the channel, then reaches a maximum which is proportional to the width, $D$.

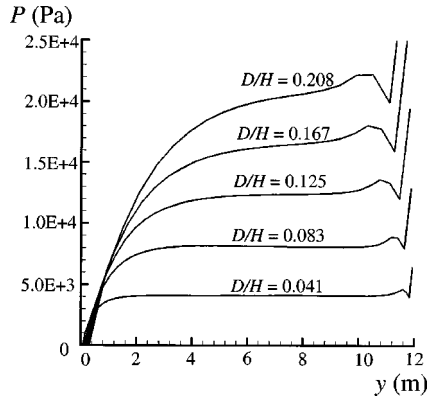


**Fig. 4 Effect of aspect ratio on pressure, $P$ (Pa), for incompressible single-phase flow, $\phi = \phi_w = 30$ deg**

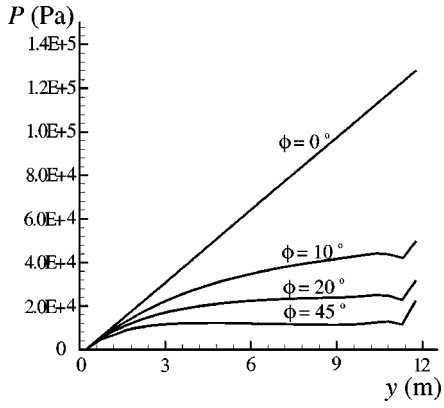


**Fig. 5 Pressure, $P$ (Pa), as a function of depth $D/H = 2{:}12$. Various angles of internal friction, $\phi$ (deg).**

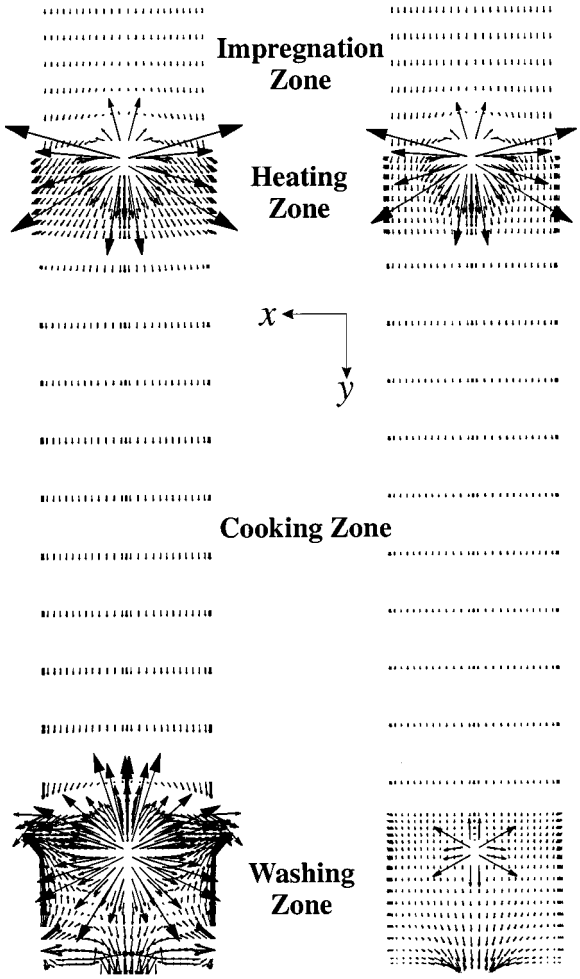


**Fig. 6 Velocity vectors, viscous/viscous compressible two-phase flow**

This class of pressure distribution is always observed for granular materials [6,13]. It differs from that observed in fluids, where the hydrostatic pressure increases linearly with depth, and is independent of the channel width.

In Fig. 5, the aspect ratio $D/H$ is fixed at 0.167, and $\phi$ is varied in the range $0 \leqslant \phi \leqslant 45$ deg with $\phi_w = \phi$. The case $\phi = 0$ deg corresponds to a frictionless material, i.e., a perfect fluid. For this case, $P$ increases linearly, reaching a maximum of $1.3 \times 10^5$ Pa at the bottom of the channel (the hydrostatic fluid pressure, with $g = 9.81$ m/s$^2$). As $\phi$ increases, the distribution departs from that for a fluid and increases asymptotically to a constant maximum, which decreases with increasing friction. The reader will note that the local pressure distortion at $y = 12$ m, Figs. 4 and 5, is due to the prescription of a fixed mass flux (velocity) at the exit.

The pressure distributions shown in Figs. 4 and 5 are in good agreement with the Janssen formula [6]. A quantitative comparison is not meaningful, owing to numerous simplifying assumptions inherent in that formula. The results illustrate the important role of shear or friction.

**Two-Phase Viscous/Viscous Compressible Solid/Fluid Flow.** Figures 6 and 7($a$) show the results for case 2, namely viscous/viscous solid/fluid flow in the apparatus of Fig. 1, generated using a grid of $72 \times 164$ cells. Figure 6 shows velocity vectors for both liquid and solid. It can be seen that for the solid, a plug-flow is apparent other than near the secondary inlets 1 and 2, where liquid injection entrains and disperses the solid particles. Liquid velocities are axial in the impregnation and cooking zones,

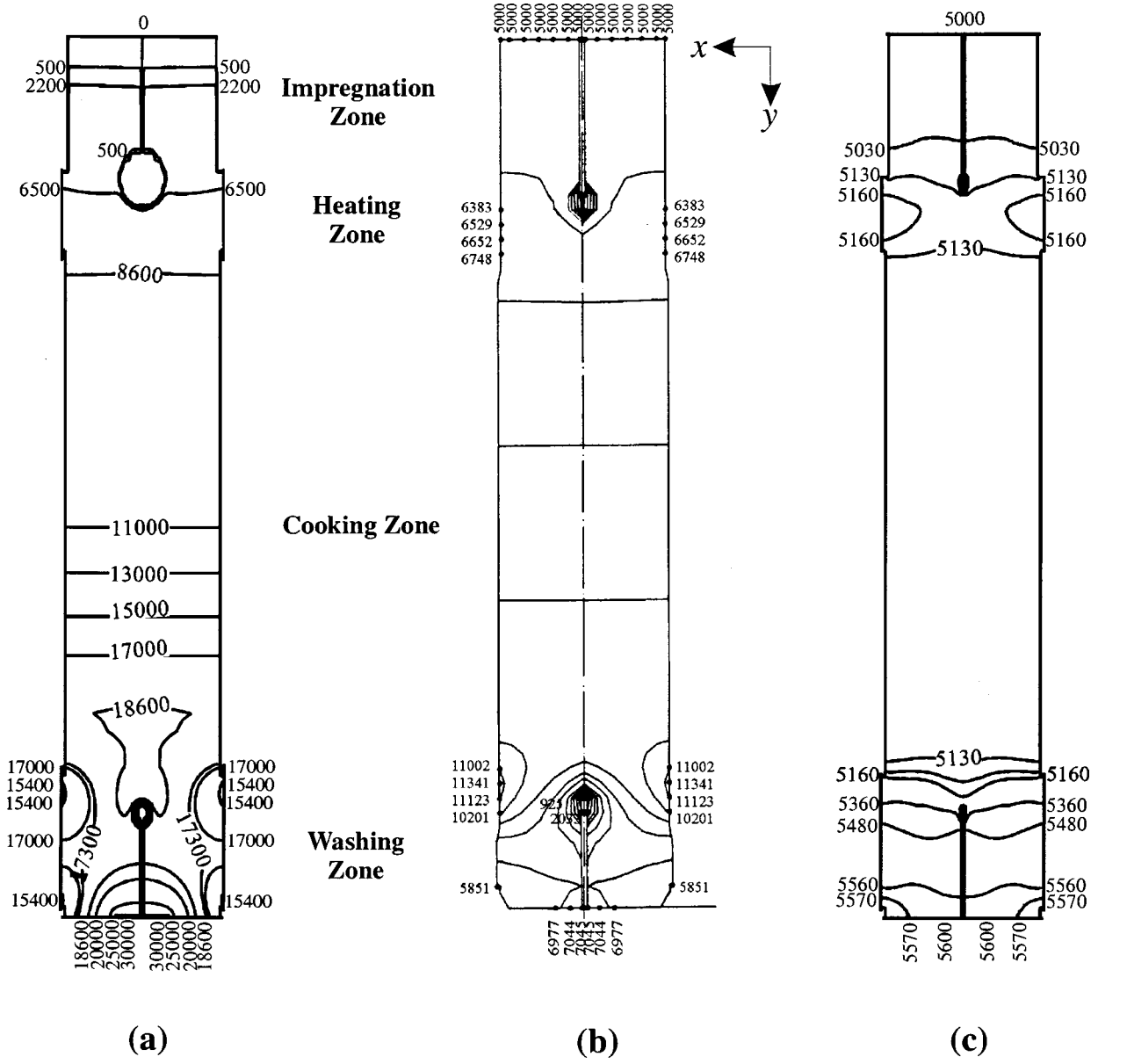


**Fig. 7 Solid pressure, *P* (Pa) contours—(*a*) viscous fluid formulation; (*b*) from Härkönen [1], with permission; (*c*) Mohr/Coulomb formulation**

but radial in the heating and washing zones near the outlet screens, due to extraction. In the upper region, solid and liquid flow co-currently while in the lower washing zone a countercurrent state is apparent at the wall, due to liquid injection at inlet 3 (see Fig. 1). The reader will note that liquid and solid phases have relatively similar densities. These spatial velocity distributions are in good agreement with those of Härkönen [1].

Figure 7(*a*) shows contours of solid pressure, *P*. The reader will note that a near linear pressure gradient is apparent in the central cooking zone, with somewhat larger gradients in the impregnation and washing zones. Though not readily apparent from Fig. 7(*a*), the pressure actually tends to zero in the vicinity of liquid injection sites 1 and 2, in addition to the main inlet. This indicates that there is no particle-to-particle contact there; i.e., the granular material is dispersed. In the impregnation zone, the compression increases slightly towards the bottom of the equipment, where a maximum of $3\times10^4$ Pa is observed. In the washing zone the pressure decreases near the side walls, due to liquid recirculation between the injection inlet 3 and outlet 2. Liquid injection and extraction in the heating and washing zones disperses the solid in these regions, and a reduction in solid volume fraction, $r_s$, and pressure, *P*, results.

Figure 7(*b*) shows the distribution of solid pressure from Härkönen [1]. These are similar to the present results, Fig. 7(*a*). Inspection of Fig. 7(*b*) reveals that *P* increases from $5\times10^3$ Pa at the main inlet to $7\times10^3$ Pa at the main outlet, with the same pressure decrease in the vicinity of the lower liquid injection screens, as noted in the foregoing. Some differences between Figs. 7(*a*) and (*b*) are observed near the main inlet and the two lateral heating and washing zones. This may be due to the fact that inertial terms, considered here, were not included in the earlier work, or because the Härkönen formulation was for an inviscid fluid; i.e., it did not contain a diffusion term within the bulk of the solid phase.

**Two-Phase Viscous/Mohr-Coulomb Compressible Solid/Fluid Flow.** Finally, the results of case 3 are presented. This case corresponds to the full solution for two-phase flow, including

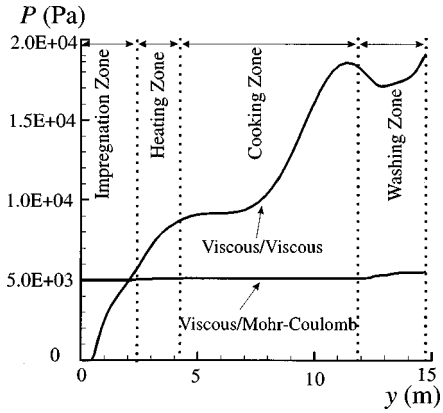


**Fig. 8 Solid-phase pressure, *P* (Pa), for viscous and Mohr-Coulomb formulations**

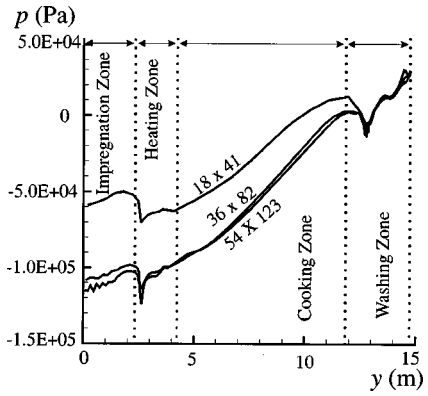


**Fig. 10 Effect of grid size**

the Mohr/Coulomb frictional behavior of the granular material. All other boundary conditions, transport properties etc. were identical to those given in case 2, above other than the solid shear viscosity, $\eta$. The angle of internal friction, $\phi$=45 deg, used in the calculation of $\eta$ is based on an industry-accepted average value.

Figure 7(*c*) shows the pressure, *P*, in the solid phase. It can be seen that *P* increases only very slightly from $5\times10^3$ Pa at the top, to $5.6\times10^3$ Pa at the bottom. For Mohr-Coulomb granular flow, the pressure is independent of height, which is in accordance with observed behavior of frictional granular materials, as discussed in the foregoing. The minor increase in each of the four zones is due to the small increases in cross section. It can also be seen that while *P* decreases near the liquid injection inlets 1 and 2 (Fig. 1), it does not approach zero, as in the previous case. This result suggests that frictional shear forces reduce dispersion of the solid particles by the pore fluid. Figure 8 is a comparison of solid pressure, *P*, midway across the reactor vessel, for case 2, viscous/viscous solid flow, and case 3, viscous/frictional Mohr-Coulomb solid. It is apparent that the two approaches generate fundamentally different profiles. For the viscous/viscous approach, the solid pressure increases from inlet to outlet (from 0 Pa to $1.8\times10^4$ Pa), in a relatively linear fashion, with depth, as expected for a Newtonian or perfect fluid. Local extrema are associated with liquid injection. Conversely, for case 3 viscous/Mohr-Coulomb formulation, the pressure is relatively constant, around $5.3\times10^3$ Pa, along the length, but is sensitive to cross-sectional size.

The effect of the angle of internal friction, on the solid pressure distribution, midway across the vessel, is shown in Fig. 9, for $\phi$=10,20,40 deg. *P* is inversely proportional to $\phi$ as demonstrated for case (1). For values of $\phi>20$ deg, the solid pressure in the impregnation zone is close to the inlet value of $5\times10^3$ Pa. For $\phi$=10 deg, gravitational forces predominate over shear forces, and the solid material is more closely packed, leading to higher solid pressures.

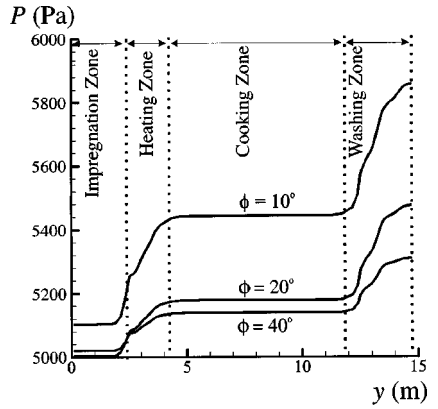


**Fig. 9 Effect of angle of internal friction, $\phi$ (deg), on the solid pressure, *P* (Pa)**

**Numerical Considerations.** The fluid pore pressure, *p*, was chosen to test for grid independence as a solved-for variable (unlike the solid pressure *P*, which is evaluated algebraically). Figure 10 shows profiles obtained using grids consisting of $18\times41(1x)$, $36\times82(2x)$ and $54\times123(3x)$ cells. The difference between inlet and outlet pressure is approximately 30 percent for the $18\times41$ and $36\times82$ grids and 3 percent for the $36\times82$ and $54\times123$ grid. Results for a $72\times164$ $(4x)$ grid are essentially identical to those for the $54\times123$ $(3x)$ grid; i.e., a satisfactory measure of grid independence is achieved.

An assessment of the effects of numerical diffusion has yet to be conducted for the current problem. It is true that higher-order numerical schemes should generate more accurate solutions; however, it is not readily apparent whether numerical considerations are the limiting factor in complex multiphase flows. The availability of 3-D multiphase direct numerical simulations (DNS) would be a useful tool in analyzing the combined effects of the precision of the discretization scheme and the accuracy of the closure assumptions.

## Conclusions

A multiphase flow model for chemical process equipment has been presented. The problem involves the simultaneous solution for two-phase flow of frictional bulk granular material and viscous liquid. The two-phase flow is driven by gravity, and the imposed solid/fluid phase discharge at the inlets and outlets. Established Eulerian algorithms were modified to perform granular flow calculations, based on the solution of systems of coupled linear algebraic equations.

The solid phase was modeled using two different approaches. In the first approach it was treated as a Newtonian fluid. The second approach extends the model to include Mohr Coulomb viscous-plastic flow. This was achieved by introducing a shear viscosity such that the stress tensor is independent of the magnitude of the rate-of-deformation tensor. In fully developed regions, where velocity gradients vanish, the viscosity coefficient is indeterminate, and the viscous-plastic threshold is reached. This, however, is a reasonable rheological behavioral assumption.

Idealized test cases showed that the present numerical scheme correctly handled the viscous-plastic regime. A solution of the full two-phase flow problem with realistic geometry and boundary conditions was then developed. The results show that the frictional properties of the solid phase play an important, previously neglected role. The solid pressure distribution down the vessel is

quite different from that obtained by neglecting friction. The present model indicated a relatively constant pressure along the vessel walls; a result which is in agreement with numerous observations of granular materials. The pressure distribution, and indeed the motion of the solid phase also appeared to be sensitive to the frictional properties of the granular material in the vicinity of fluid inlets, a situation with important ramifications to the equipment designer and operator.


## Acknowledgments

The authors acknowledge the assistance of the staff of Ahlstrom Machinery Inc., of Glens Falls, NY. and in particular Mr. Aaron Leavitt. The advice and support of Dr. Donald Singleton and Mr. Ron Jerome at NRC, are gratefully acknowledged.


## Nomenclature

$A, B, m$ = coefficients in equation of state
$b$ = Forchheimer's constant
$D$ = diameter or width
$d_0$ = threshold rate of deformation
$d_{ij}$ = components of deformation rate tensor
$d_{\mathrm{I}}, d_{\mathrm{II}}$ = principle rates of deformation
$\vec{g}$ = acceleration due to gravity
$H$ = height
$k$ = permeability
$k'$ = interphase slip coefficient
$P, p$ = solid, fluid pressure
$r_f, r_s$ = fluid, solid volume fraction
$\boldsymbol{\mu}$ = velocity vector
$u, v$ = velocity components
$\mathbf{u}_f, \mathbf{u}_s$ = fluid, solid phase velocity
$x, y$ = displacement
$\Delta$ = rate of deformation
$\eta, \mu$ = solid, fluid viscosity
$\kappa$ = Kappa
$\rho, \rho_f, \rho_s$ = density, fluid density, solid density
$\sigma$ = normal stress
$\bar{\bar{\sigma}}$ = stress tensor
$\sigma_{11}, \sigma_{22}, \sigma_{xx}, \sigma_{yy}$ = normal components of stress tensor
$\sigma_{\mathrm{I}}, \sigma_{\mathrm{II}}$ = principle stresses
$\tau$ = shear stress
$\tau_{12}, \tau_{xy}$ = shear component of stress tensor
$\tau_w$ = wall shear stress
$\phi$ = angle of internal friction
$\phi_w$ = angle of friction with wall
$\psi$ = angle of major principle stress
$\partial u/\partial n$ = wall velocity gradient

## References


[1] Härkönen, E. J., 1984, ''A Mathematical Model for Two-Phase Flow. Acta Polytechnica Scandinavica,'' Mech. Eng. Ser., No. 88.
[2] Härkönen, E. J., 1987, ''A Mathematical Model for Two-Phase Flow, in a Continuous Digester,'' Tappi J., Dec., pp. 122–126.
[3] Scheidegger, A. E., 1974, *The Physics of Flow Through Porous Media*, 3rd Ed. University of Toronto Press, Toronto, ON, Canada.
[4] Michelsen, F., and Foss, B., 1996, ''A Comprehensive Mechanistic Model of a Continuous Kamyr Digester,'' Appl. Math. Model., **20**, pp. 523–533.
[5] Saltin, J. F., 1992, ''A Predictive Dynamic Model for Continuous Digesters,'' Proc TAPPI Pulping Conference, Boston, MA, pp. 261–267.
[6] Brown, R. L., and Richards, J. C., 1970, *Principles of Powder Mechanics*, Pergamon, Oxford, UK.
[7] Drucker, D. C., and Prager, W., 1952, ''Soil Mechanics and Plastic Analysis of Limit Design,'' Quarterly Appl. Math., **10**, pp. 157–165.
[8] Scott, R. F., 1963, *Principles of Soil Mechanics*, Addison-Wesley, Reading, PA.
[9] Savage, S. B., 1984, ''The Mechanics of Granular Flow,'' Adv. Appl. Mech., **24**, pp. 289–366.
[10] Savage, S. B., 1998, ''Analyses of Slow High-concentration flows of Granular Materials,'' J. Fluid Mech., **377**, pp. 1–26.
[11] Patankar, S. V., 1980, *Numerical Heat Transfer*, Hemisphere, New York, NY.
[12] Spalding, D. B., 1980, ''Numerical Computation of Multiphase Fluid Flow and Heat Transfer,'' *Recent Advances in Numerical Methods in Fluids*, ed., C. Taylor, Vol. 8, pp. 139–167.
[13] Shamlou, P. A., 1988, *Handling of Bulk Solids, Theory and Practice*, Butterworth & Co., London, UK.